Ocean Engineering 261 (2022) 112046

Contents lists available at ScienceDirect

Ocean Engineering

journal homepage: www.elsevier.com/locate/oceaneng

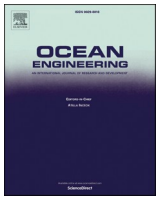

Investigation of blade-mast fluid-structure interaction of a tidal turbine

Corentin Lothode [a,*], Jules Poncin [b], Didier Lemosse [c], David Gross [b], Eduardo Souza de Cursi [c]

[a] LMRS, UMR 6085 (CNRS, Université de Rouen), Avenue de l'Université, 76800, Saint-Étienne du Rouvray, France
[b] K-Epsilon, 1300 route des crêtes, 06560, Sophia, Antipolis, France
[c] LMN, INSA Rouen, Avenue de l'Université, 76800, Saint-Étienne du Rouvray, France

ARTICLE INFO

Keywords:
Marine Renewable Energy (MRE)
Tidal turbine
Flexible blades
Fluid-Structure Interaction (FSI)
Computational Fluid Dynamics (CFD)

ABSTRACT

In this article, we investigate the movement and vibrations of a blade due to the presence of the mast. When the blade passes in front of the mast, a sudden pressure spike induces vibrations in the blade. To study the influence of stiffness, two different structures were studied. We present our numerical schemes concerning the resolution of the flow, the behavior of the structure and the coupling of the two systems. Then, we validate two methods against an experiment (Bahaj et al., 2007). In a third section, we present cases of fluid-structure interaction. Several structures are setup by modifying the stiffness of the material. Their steady open-water (without a mast) behaviors are compared. And finally, two dynamic fluid-structure computations are performed to compare the behavior of an elastic blade passing next to a mast. For all the cases, we use K–FSI developed by K-Epsilon to solve the fluid-structure interaction (FSI).

1. Introduction

Tidal currents as a potential source of renewable energy has been under study for more than 10 years now. Mainly horizontal tidal turbines have been investigated both numerically and experimentally (Bahaj et al., 2007; Mycek et al., 2014; Tedds et al., 2014; de Jesus Henriques et al., 2014; Fernandez-Rodriguez et al., 2014). Vertical tidal turbines have also being studied (Stallard et al., 2013; Derakhshan et al., 2017). Two designs were also compared extensively in the literature, see (Khan et al., 2009) for example. Current research focuses on optimizing array of tidal turbines and their interaction (Funke et al., 2014), erosion of the seabed (Verbeek et al., 2020), performance and optimization of the shape or structure (Nicholls-Lee, 2011), fatigue and reliability (Finnegan et al., 2020).

To optimize the performance of a tidal turbine, there is a need for accurate and efficient tools to perform simulations. In this article, we focus on the development and evaluation of a new tool to better understand the physics and calculate the loads acting on a single flexible tidal turbine including mast effects. This tool could be used to improve estimations of fatigue for example.

The first simulation framework used to perform computations was the Blade Element Momentum Theory (BEMT), for example in Batten et al. (2007)). BEMT is a good approach to assess the open water performance of one turbine, but it fails to accurately simulate the performance in the presence of obstacles or other turbines. To avoid this problem, other approaches have been developed such as the Vortex Lattice Method (VLM) in Pinon et al. (2012). Their focus is the wake of the turbine to study the interaction between two or more turbines (for example in Mycek et al. (2013)). Their results are accurate until stall which is a known limitation of the model: their method force the flow to be attached until the trailing edge, hence overestimating hydrodynamical forces.

Attempts to use Computational Fluid Dynamics (CFD) on wind or tidal turbine has been made in the past. To avoid too much computational efforts, many authors modeled the behavior of the turbine instead of solving the complete geometry. For instance, Jimenez et al. (2007) used Large Eddy Simulation (LES) with the turbine modeled by an approximate model of a concentrated drag force to study the wake development. Also using an approximate model for the turbine, Calaf et al. (2010) performed a LES computation using an actuator disk.

Fully resolved blade geometry CFD computations are computationally expensive but can yield much more information about the flow behavior and force distribution along the blade. Afgan et al. (2013) modeled the fluid using different turbulence models ($k - \omega$ SST,

* Corresponding author.
E-mail addresses: corentin.lothode@univ-rouen.fr (C. Lothode), jules@k-epsilon.com (J. Poncin), david@k-epsilon.com (D. Gross), eduardo.souza@insa-rouen.fr (E. Souza de Cursi).
URL: https://didier.lemosse@insa-rouen.fr (D. Lemosse).

https://doi.org/10.1016/j.oceaneng.2022.112046
Received 12 May 2020; Received in revised form 29 June 2022; Accepted 16 July 2022
Available online 3 August 2022

Launder-Reece-Rodi and LES) on the 20° pitch angle case of Bahaj et al. (2007). They performed unsteady simulations including the mast and a simplified geometry of the cavitation tunnel. Yan et al. (2017) was the first work to perform a full-scale free-surface flow simulation of a tidal turbine. All of those methods need a lot of computing power, and are only slightly more accurate than BEMT if the goal is only to obtain information on performance curves. Their main advantage is their ability to add geometry details (mast, cables, proximity to the seabed or duct for example) that would be difficult or even impossible to model with current BEMT models. To account for the fluid when simulating an unsteady simulation, a linear model is often used. This is, for example, what is used by the industry standard software *Bladed* and the open-source software *FAST* (Jonkman, 2010). It is with the work of Bazilevs et al. (2011) and Takizawa et al. (2011) that the first dynamic FSI computations were performed on wind turbines using CFD on fully resolved geometries.

Tidal and wind turbines are different when considering fluid-structure interaction in the sense that water has a density of three order of magnitude higher than air. The fluid-structure coupling is therefore much greater and comparable to what can be observed for hydrofoils Lothodé et al. (2013). Murray et al. (2018) investigated the influence of the added mass on the response behavior of tidal turbines in order to model it in a BEMT code. They showed that the natural frequency is decreased especially when using light blades. Turbulence influx events could not induce vibration because their frequency was higher than the natural frequency of the blade. Nicholls-Lee (2011) coupled a structure solver with a surface panel code in order to obtain a steady-state solution and to optimize a tidal turbine structure. Zilic De Arcos et al. (2019) studied the performance and deflection of a turbine with flexible blades using two-way coupling, but no dynamic effects were investigated. However, no study of the interaction between the various elements of the tidal turbine has been carried out. Therefore, understanding what happens for a blade-mast interaction including the effects due to flexible blades involves the use of strongly coupled fluid-structure interaction solver. For example, these results could be used to understand the dynamics of passively adaptive blades (Nicholls-Lee et al., 2013).

We first present our numerical schemes. The fluid solver is described in Section 2.1 and the structure solver is detailed in Section 2.2. Our fluid-structure coupling scheme is shown in Section 2.3 and finally mesh morphing is quickly introduced in Section 2.4. Next, we validate our simulation procedure in Section 3.3, first ignoring blade deformation using Bahaj et al. (2007) as a baseline validation for rigid geometry. Later, we introduce the different structures used in the article and reproduce the performance curve taking into account the flexibility of the blades in Section 3.4. Finally, simulations of two different structures focusing on the blade-mast interaction are discussed in Section 4.

2. Numerical method

In this section, we describe the different solvers used in this article and the coupling scheme that allows to solve the steady and unsteady simulations. In Fig. 1, we show a schematic of the domain and we describe the different notations used in this article in Table 1.

2.1. Fluid solver

The fluid solver is ISIS-CFD (Deng et al., 2005). It is developed by the METHRIC team of LHEEA laboratory and commercialized by Cadence. It is included in FINETM/Marine. ISIS-CFD solves the incompressible unsteady Reynolds Averaged Navier-Stokes equations. The code is fully parallel using the MPI (Message Passing Interface) protocol.

It is formulated through a fully unstructured finite-volume method to obtain the spatial discretization of the conservation equations. Arbitrarily shaped polyhedrons are assembled through a list of faces. All unknown variables are cell-centered.

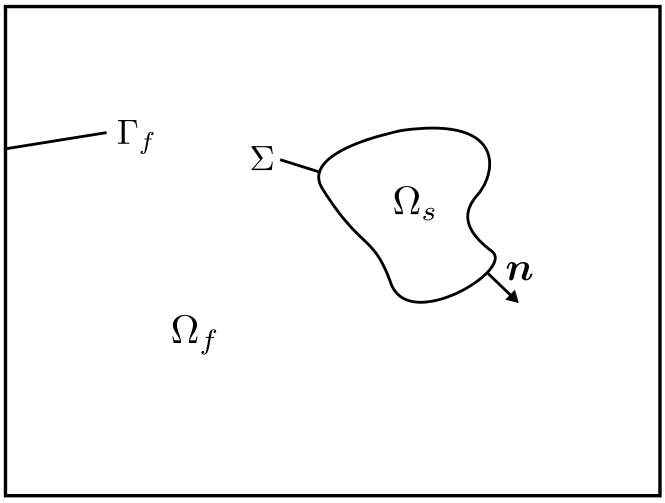

Fig. 1. Notations used for the fluid-structure domain.

Table 1
Notations for the fluid domain, structure domain and interface (see Fig. 1).

Symbol	Description
Ω	complete domain $\Omega = \Omega_f \cup \Omega_s$
Ω_f	fluid domain
Ω_s	structure domain
Σ	fluid-structure interface, $\Sigma = \Omega_f \cap \Omega_s$
Γ_f	fluid boundaries
$\boldsymbol{n}$	normal outer vector

The temporal integration scheme is the implicit, second order Backward Differentiation Formula (BDF2) scheme when dealing with unsteady configurations. For each time step, the residual of the errors is minimized through an inner loop in order to solve the non-linearities of the system. Pressure-velocity coupling is enforced by a SIMPLE like algorithm: at each time step, the velocity updates come from the momentum equation and the pressure is given by the mass conservation law.

Turbulence is accounted using additional transport equations for modeled variables. They are solved in a form similar to the momentum equations and they can be discretized and solved using the same principles (Duvigneau et al., 2003). In this article, we use the $k-\omega$ SST model, a two-equations eddy-viscosity model.

An Arbitrary Lagrangian Eulerian (ALE) formulation is used to account for fluid mesh changes due to the body deformation (Hughes et al., 1981; Leroyer and Visonneau, 2005). Basically, the flow velocity $\boldsymbol{u}_{\text{fluid}}$ is decomposed in two velocities: a velocity of the mesh $\boldsymbol{u}_{\text{mesh}}$, and an additional velocity relative to the mesh $\boldsymbol{u}_{\text{relative}}$.

$$\boldsymbol{u}_{\text{fluid}} = \boldsymbol{u}_{\text{mesh}} + \boldsymbol{u}_{\text{relative}} \tag{1}$$

It is possible to have a non-matching sliding interface (Queutey et al., 2012). It allows to have a rotating mesh inside a fixed mesh for example, and to avoid using more costly procedures involved in overlapping meshes. This is very useful for modeling a propeller or a tidal turbine.

A procedure called Rotating Frame Method (RFM) is available. It adds a mesh velocity corresponding to a rotation in a domain whilst the mesh stays fixed. It allows to compute performance curves with larger time steps than typical rotating mesh methods. A comparison of the two methods is made in Section 3.4.

2.2. Structure solver

We use the solver K-Struct which is developed by the company K-

Epsilon (K-Epsilon, 2020). The solver is based on a non-linear finite element formulation derived through the use of the virtual work principle. The temporal discretization is driven by a Newmark–Bossak scheme (Wood et al., 1980) and the resolution is ensured by a Newton method through the computation of the tangent matrix. Non-linear iterations are relaxed with an Aitken acceleration.

The code initially aimed to simulate the dynamic behavior of sailboat rigging: sails, mast and cables (Durand et al., 2014). A non-linear finite element method with a large displacement formulation is implemented. While numerous element types have been implemented in the structural code, in the present study, only Euler-Bernoulli beam elements are used, as shear deformation was considered negligible. This element accounts for torsion, bending and axial deformations. It offers a good compromise between accuracy and solving speed compared to more complex shell elements. This kind of element is used in the industry standard software *FAST* (Wang et al., 2017). The topology and properties of the different structures used in this work will be further detailed in Section 4.

2.3. Coupling scheme

We use K–FSI, a FSI software developed by K-Epsilon. K–FSI implements a strong coupling scheme, more details are given in Durand (2012). As stated previously, the coupling was first developed to tackle sails and rigging issues. Even though air is not a dense material, sails have a large wetted area and are lightweight structures. As shown in Causin et al. (2005), large wetted areas and light structures induce strongly coupled fluid-structure problems. In the case of a tidal turbine, the material used can be dense (typically metals), but the wetted area is significant and the surrounding fluid is denser than air (about 10^3 times more). It follows that the problem is also strongly coupled.

To tackle strongly coupled problems, numerous solutions exist (Fernández, 2011). Most of them are partitioned algorithms where the fluid problem and the structure problem are solved separately. The most naive algorithm is often referred as explicit: during one time step, the fluid problem and the structure problem are solved only once, one after each other. It is the fastest and simplest algorithm for weakly coupled problems, but it is unstable in the case of strongly coupled cases. Monolithic schemes, where all the equations are solved together, can be very stable. Since all equations must be developed in a similar framework, and all unknowns are shared between systems, they make it more difficult to use already existing software.

In the case of partitioned schemes used for strongly coupled cases, an implicit scheme with a relaxation (applied to forces given by the fluid or position of the nodes given by the structure) can be stable if the relaxation rate is low enough (Causin et al., 2005). During one time step, the fluid equations and the structure equations are solved one after another until a convergence is reached. It can be very costly if the convergence is not fast enough. The choice of the relaxation rate is a matter of trade-off between greater stability and convergence rate. An Aitken procedure is useful for dynamically adjusting the relaxation rate and accelerating convergence, as in (Küttler and Wall, 2008).

Instead of solving a fixed point problem to reduce the residual of errors between the structure and fluid forces, one can use a Newton algorithm including an exact Jacobian operator as in (Fernández and Moubachir, 2005). It turned out to be very efficient, even though the fluid-structure problem was greatly simplified in order to be able to develop such an operator. K–FSI takes advantage of this idea to accelerate convergence. Such operators have been developed in Lothodé (2018). For example, it allowed to solve problems on membranes (Gross, 2015) or vortex induced vibrations on offshore risers (Lothodé et al., 2015).

Forces (stresses on the wetted surface) are given through an arbitrary polygonal surface mesh by the fluid solver. They are interpolated on the structure by projecting the force vector onto the neutral axis of the beam.

$$\boldsymbol{f}^{(i,n)}_{\text{structure}} = P^{i\mapsto s}\left(\boldsymbol{f}^{(i,n)}_{\text{interface}}\right) \tag{2}$$

In between two beam nodes, a linear interpolation is done for the torsion and deflection depending on the position of the projected forces. The displacements of the structure (at a time step i and sub-iteration n: $\delta\boldsymbol{x}^{(i,n)}_{\text{structure}}$) are propagated to the interface surface mesh through a cubic spline representing the neutral axis of the beam with $P^{s\mapsto i}$ the operator mapping the structure position to the interface position:

$$\boldsymbol{x}^{(i,n)}_{\text{interface}} = P^{s\mapsto i}\left(\boldsymbol{x}^{(i,n-1)}_{\text{structure}} + \delta\boldsymbol{x}^{(i,n)}_{\text{structure}}\right) \tag{3}$$

Once the structure has moved the interface surface mesh, a comparison is done between the old position of the surface nodes and the new ones:

$$\delta\boldsymbol{x}^{(i,n)}_{\text{interface}} = \boldsymbol{x}^{(i,n)}_{\text{interface}} - \boldsymbol{x}^{(i,n-1)}_{\text{interface}} \tag{4}$$

If the maximum observed displacement of the interface nodes is non-zero:

$$\delta\boldsymbol{x}^{(i,n)}_{\text{interface}_\infty} > \epsilon_{\text{displacement}} \tag{5}$$

a mesh-morphing algorithm is performed to modify the position of all the nodes in the volume in order to maintain a good quality mesh. The algorithm is described in **Algorithm 1**. A mesh movement velocity $\boldsymbol{u}^{i,n)}_{\text{mesh}}$ is computed from the new position of the mesh and used through the ALE capability of the fluid solver.

Algorithm 1. Quasi-monolithic algorithm.

while $t_i < t_{final}$ **do**
  $i \leftarrow i + 1$;
  $t_i \leftarrow t_{i-1} + \Delta t$;
  $n \leftarrow 0$;
  distribution of $\boldsymbol{f}^{(i-1,n_{\text{final}})}_{\text{fluid}}$ on the structure ;
  update structure $\delta\boldsymbol{x}^{(i,n)}_{\text{structure}}$;
  deform mesh according to $\delta\boldsymbol{x}^{(i,n)}_{\text{interface}}$;
  compute $\boldsymbol{u}^{(i,n)}_{\text{mesh}}$;
  while $\left\|r^{(i,n)}_{fluid}\right\| < \varepsilon$ **do**
    $n \leftarrow n + 1$;
    update linearly $\boldsymbol{u}^{(i,n)}_{\text{fluid}}$ and $\boldsymbol{p}^{(i,n)}_{\text{fluid}}$ using $\boldsymbol{u}^{(i,n-1)}_{\text{mesh}}$;
    compute $\left\|r^{(i,n)}_{\text{fluid}}\right\|$;
    compute $\boldsymbol{f}^{(i,n)}_{\text{fluid}}$;
    distribution of $\boldsymbol{f}^{(i,n)}_{\text{fluid}}$ on the structure ;
    update structure $\delta\boldsymbol{x}^{(i,n)}_{\text{structure}}$;
    deform mesh according to $\delta\boldsymbol{x}^{(i,n)}_{\text{interface}}$;
    compute $\boldsymbol{u}^{(i,n)}_{\text{mesh}}$;
  end
end

2.4. Mesh morphing

After the interface deformation, the whole of the fluid mesh needs to be moved. This deformation occurs at each coupling iteration. The number of calls to this procedure being non-negligible, the mesh deformation needs to be fast. For this purpose, a method has been developed which propagates the deformation state to the fluid mesh. The basic principle is to propagate, from the interface to the boundaries, the information about displacements. A smoothing step can be needed to improve the quality of the cells. The details of the method are given in Durand (2012).

3. Fluid validations

3.1. Description of the reference case

In Bahaj et al. (2007), the authors describe an experiment of a small-scale tidal turbine. The tests were carried out in a cavitation tunnel at the University of Southampton (see Fig. 2). The rotor radius of the turbine is $r = 400$ mm. It was chosen as a compromise between maximizing the Reynolds number and reducing the tunnel blockage correction.

In the original work, the blockage correction is based on an actuator disk model of the flow through the turbine in which the flow is presumed to be uniform across any cross-section of the stream tube enclosing the turbine disc. For example, with a single rotor and a thrust coefficient of 0.8, the corrections amounted up to an 18% decrease in power coefficient and an 11% decrease in thrust coefficient.

All the curves presented in this article take into account this blockage correction. It means that all results are presented as open water curves. These numerical computations are open water computations and no correction are necessary.

The blades are made out of the NACA 63-8xx series. The distribution of pitch, thickness and chord can be found in Table 2. The pitch angle reference is the angle of the section $r = 80$ mm. It means that a pitch of 15° is simply taking the blade untouched and 20° means adding a rotation of 5° to the blade.

To compare the performance of the tidal turbine, we introduce three dimensionless quantities. The thrust coefficient C_T is equal to the force in the flow direction divided by $\frac{1}{2}\rho V^2 S$. The power coefficient C_P is equal to the torque times the rotation speed divided by $\frac{1}{2}\rho V^3 S$. The tip speed ratio, TSR, is the ratio of blade tip speed to flow speed. These notations and definitions are reported in Table 3 ρ is the density of the fluid (here 998.3 kg/m^3). r is the radius of the turbine (here 0.4 m).

3.2. Description of the simulations

The fluid domain is decomposed in two parts. The outer domain is made of a box of width $L_x = 4$ m, length $L_y = 6$ m and height $L_z = 4$ m. A smaller domain, cylindrical, represents the domain in rotation and has a length of $L_y^{'} = 0.6$ m and a radius of $r' = 0.6$ m. It includes the hub part that is rotating and the blades. The two domains are shown in Fig. 3. The inner domain can rotate inside the outer domain. The two domains are linked through a sliding interface. The mesh is generated with HexpressTM, part of FINETM/Marine, with an octree method and consists of 4.1 million hexagonal cells.

Fig. 2. Photo of the experiment (from Bahaj et al. (2007)).

Table 2
Blade geometry description.

r (*mm*)	c/R	Pitch (°)	t/c (%)
80	0.125	15	24
100	0.1203	12.1	22.5
120	0.1156	9.5	20.7
140	0.1109	7.6	19.5
160	0.1063	6.1	18.7
180	0.1016	4.9	18.1
200	0.0969	3.9	17.6
220	0.0922	3.1	17.1
240	0.0875	2.4	16.6
260	0.0828	1.9	16.1
280	0.0781	1.5	15.6
300	0.0734	1.2	15.1
320	0.0688	0.9	14
340	0.0641	0.6	14.6
360	0.0594	0.4	13.6
380	0.0547	0.2	13.1
400	0.05	0	12.6

Table 3
Notations used for the dimension and dimensionless numbers.

Name	Property
r	radius of the turbine (m)
$S = \pi r^2$	swept area (m^2)
V	inlet velocity (m/s)
ρ	density of the fluid (kg/m^3)
Q	turbine torque (Nm)
T	turbine drag (N)
Ω	rotation speed (rad/s)
$TSR = \frac{\Omega r}{V}$	tip speed ratio
$C_T = \frac{T}{\frac{1}{2}\rho V^2 S}$	thrust coefficient
$C_P = \frac{Q \times \Omega}{\frac{1}{2}\rho V^3 S}$	power coefficient

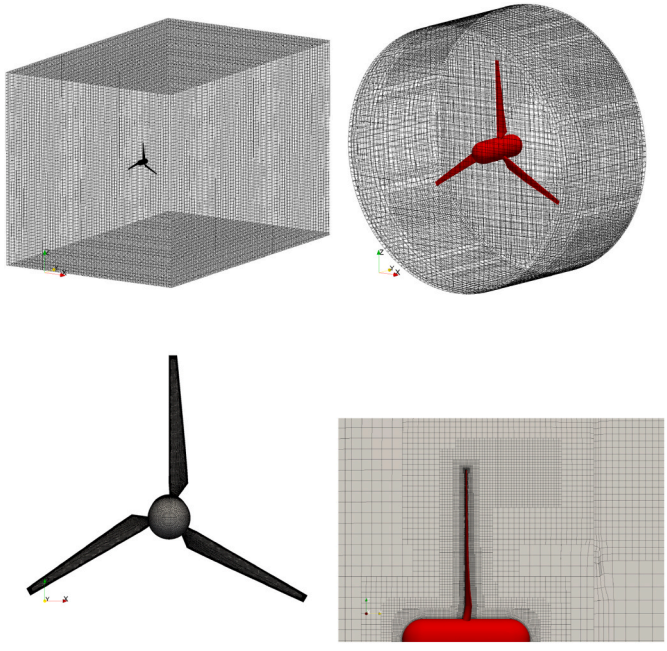

Fig. 3. Different views of the fluid mesh. From left to right, top to bottom: computational domain, internal cylindrical domain (used as a sliding interface), tidal surface mesh, volume mesh cut.

The boundary layer is captured with a $y_+ \approx 30$, thanks to the insertion of cell layers. Depending on the surface, 10 to 20 layers were added in order to reach the needed size, with a geometric expansion law with a factor of 1.2 increase in thickness between each pair of layers. Refinement boxes were placed to capture the tip vortices and the close wake correctly.

Finally, an orthogonality criterion was setup for the mesh optimization step (smoothing) of 20°. The mesh refinement size was chosen in order to satisfy both best practices and constraints on the allocated CPU time of the project. As shown in the next section, the mesh yields satisfactory results even if a mesh independence should be pursued in future research.

The sides and outlet boundary conditions use a zero-gradient boundary condition for pressure ($\nabla p \cdot \boldsymbol{n} = 0$). The inlet boundary condition is an imposed velocity of $\boldsymbol{u}_{\text{fluid}} = V$.

With the Rotating Frame Method, a rotation mesh velocity is added to the cylinder through the ALE formulation ($\boldsymbol{u}_{\text{mesh}} = \Omega \|\boldsymbol{d}\|_2$ with $\boldsymbol{d}$ the distance perpendicular to the rotation axis) while the mesh if physically fixed:

$$\frac{\partial \boldsymbol{x}_{\text{mesh}}}{\partial t} = 0 \tag{6}$$

In other words, the mesh velocity is not computed from the mesh movement, because it is fixed, but is imposed as if the mesh was rotating. With this method, the wake shows a steady behavior. The time step only plays a role for the convergence toward the steady solution and therefore can be very large.

With the dynamically rotating mesh, the mesh is rotating at an imposed velocity. The fluid velocity is not imposed, instead the mesh velocity is computed from the mesh movement:

$$\boldsymbol{u}_{\text{mesh}} = \frac{\partial \boldsymbol{x}_{\text{mesh}}}{\partial t} \tag{7}$$

The derivative is approximated through a Backward Differentiation Formula of order one or two. In this case, the wake is unsteady from the point of view of the observer. Both methods exploit the ALE capability of the fluid solver, but in a different manner.

When the mast is included in the domain, the Rotating Frame Method cannot be used accurately anymore, and only the dynamically rotating mesh can be used.

3.3. Validating all pitches

To validate our fluid model, we perform the five runs listed in Table 4 using the Rotating Frame Method. A time step of $\Delta t = 1/20^{th}$ of a rotation $\left(\Delta t = \frac{1}{20}\frac{V \times TSR}{r \times 2\pi}\right)$ is used, and iterations continue until convergence is reached. For each pitch angle, seven TSR are simulated (4, 4.5, 5, 5.5, 6, 7 and 8). Results are shown in Fig. 4.

The blade pitch angle of 15° corresponds to the highest angle of attack. The flow around the blade is fully separated at a TSR of 3 and still partially detached for a TSR from 4 to 5. For TSR between 4.5 and 5.5, the error observed between the experimental data and the simulation is about 5% for the C_P and 2% for the C_T. Outside this range, the error is larger, especially for high TSR where the experimental C_P drops quicker than what is observed with the simulations. The observed C_P peak is observed for a TSR of 5, which matches the experimental peak, with a slightly larger value (0.4626 for the simulation, 0.44 for the experiment).

Table 4
Pitch angle and corresponding flow speed.

Pitch angle (°)	Flow speed
15°	1.40 m/s
20°	1.73 m/s
25°	1.54 m/s
27°	1.30 m/s
30°	1.54 m/s

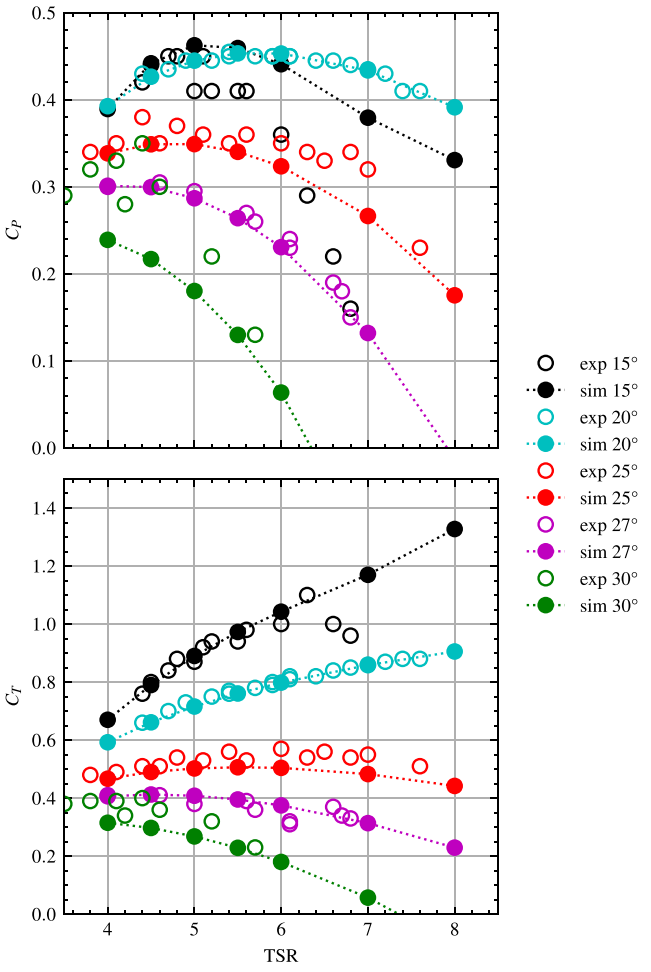

Fig. 4. Power and thrust coefficients for all cases in Table 4 with the Rotating Frame Method. Simulations are displayed with solid circular markers connected by a dotted line and experiment data are displayed with empty circular markers.

The blade pitch angle of 20° corresponds to the design (optimum) angle. The flow is only partially detached for a TSR of 3 on the upper part of the blade, and fully separated for the other half of the blade. Some detached flow can still be seen for TSR up to 4.5, but is limited to a small area of the blade. The error made between the experimental and the simulation results is very small (about 1% for both C_P and C_T). It is probably due to an accurate blockage correction, and an attached flow behavior around the blades. The C_P peak is not as clear as the one with an angle of 15°, and occurs at a TSR of 5.5 ($C_P = 0.4533$), although the value obtained for a TSR of 5 and 6 are close (0.4450 and 0.4531 respectively).

The blade pitch angle of 25° is starting to show a significant loss in term of power peak, and it is even worse for the blade pitch angles of 27° and 30°. With the angle of 25°, the flow behavior is similar to the blade pitch angle of 20° with only the lower third part of the blade showing separation. For the blade pitch angles of 27° and 30°, this separation is even smaller. For the blade pitch angle of 30°, the flow starts to separate at the tip, on the front side. The difference observed between the simulation and the experiment is only significant for the blade pitch angle of 30°, otherwise the agreement is good (less than 5% difference). For the blade pitch angles of 25°, 27° and 30°, the C_P peaks at a TSR of 5, 4 and 4 respectively, with a C_P of 0.3491, 0.3012 and 0.2391.

3.4. Comparison between RFM and dynamic rotating mesh

The goal of this section is to introduce a moving rotating mesh and to study the time step that should be used in this case. We use the same domain and mesh as in Section 3.3. In the case of a RFM computation, the best practice Numeca (2018) is to use a time step of a $1/20^{th}$ of a rotation. In the case of a dynamic rotating mesh (DRM), we tried two time steps: $1/100^{th}$ and $1/200^{th}$ of a rotation.

Performing a first set of computations using the best practices, the first results obtained were different and are shown in full and dashed lines in Fig. 5. A second set of DRM computations was launched using a time step of $1/200^{th}$ of a rotation, and the results were in agreement with the RFM and with the experiment, see dotted line in Fig. 5. The remaining difference is due to the unsteady behavior of the flow that is described with a better accuracy in the case of the DRM computation. In addition, the wake of the rotor outside the cylindrical inner domain is different when using DRM computations because the position of the turbine change with time whereas in the case of RFM it does not. In conclusion, the use of a time step below a $1/200^{th}$ of a rotation should be used in the case of a DRM computation. Reducing the time step size further would lead to a greater computational effort.

4. Fluid-structure computations

For all fluid-structure computations, the pitch angle used is 20° and the flow speed is $V = 1.73$ m/s, as it was the design angle for this tidal turbine.

4.1. Description of the structure

In the case of the experiment from Bahaj et al. (2007), the blades are made of solid aluminum and appears to be rigid. In order to have more flexible structures, we modeled the structure as a restricted section of the blade, using a beam inside the blade. The structure box is located at the largest part of the profile (see Fig. 6).

The root of the blade is rendered rigid in our computations at a radius smaller than 0.08 m, in grey in Fig. 7. For the structure labeled as E_4, we used a Young modulus of 69 GPa, corresponding to aluminum. The Poisson's ratio is 0.35. We introduce two other Young moduli:$E_2 = \frac{E_4}{2}$ and $E_1 = \frac{E_4}{4}$. The results using the module Young labeled E_4 are referred to as E_4. We do the same for E_2 and E_1.

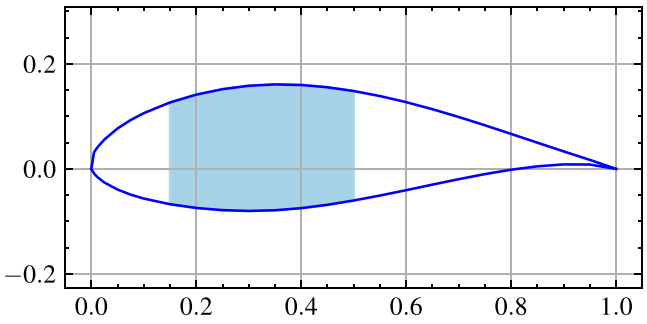

Fig. 6. The box reinforced in blue for section at $r = 80$ mm. (For interpretation of the references to colour in this figure legend, the reader is referred to the Web version of this article.)

In the local frame of the beam, x is the direction of the neutral axis, y is orthogonal of x and corresponds to the flap-wise direction, z is orthogonal to x and y and corresponds to the turbine rotation axis. The properties of the beam are given with the notations in Table 5.

The obtained properties are shown in Fig. 7. As E is constant, and the other quantities vary for each cross section, we chose to show $E \times S$, the axial stiffness, $E \times I_y$ the flap wise bending stiffness, $E \times I_z$ the rotation wise bending stiffness, and $G \times J$ the torsional stiffness.

4.2. Quasi-static computation

The performance curves were obtained for different structures using quasi-static computations. A quasi-static computation consists of running a long steady fluid computation, then after each convergence of the fluid forces, those forces are applied to the structure and the new structural position is computed using a steady state scheme. After a few iterations, the forces between the structure and the fluid are in equilibrium. The obtained result is a steady state.

In Fig. 8, we can see that the results between the fixed computation and E_4 are close. The C_T is a little bit superior, but the C_P is similar. E_2 and E_4 are also showing an increasing C_T, but there is a decay for high TSR, because the blade aligns itself with the flow. C_P performances

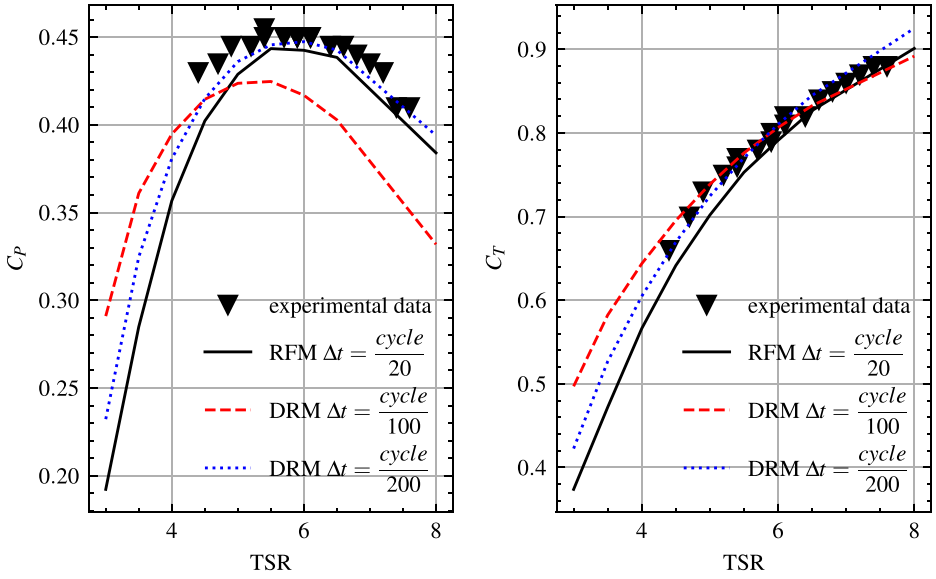

Fig. 5. Comparison between RFM and DRM. Full line, dashed line and dotted line represents results obtained respectively with the RFM method, with a rotating mesh with a time step of $\Delta t = \frac{cycle}{100}$ and with $\Delta t = \frac{cycle}{200}$. Markers are experimental results from Bahaj et al. (2007).

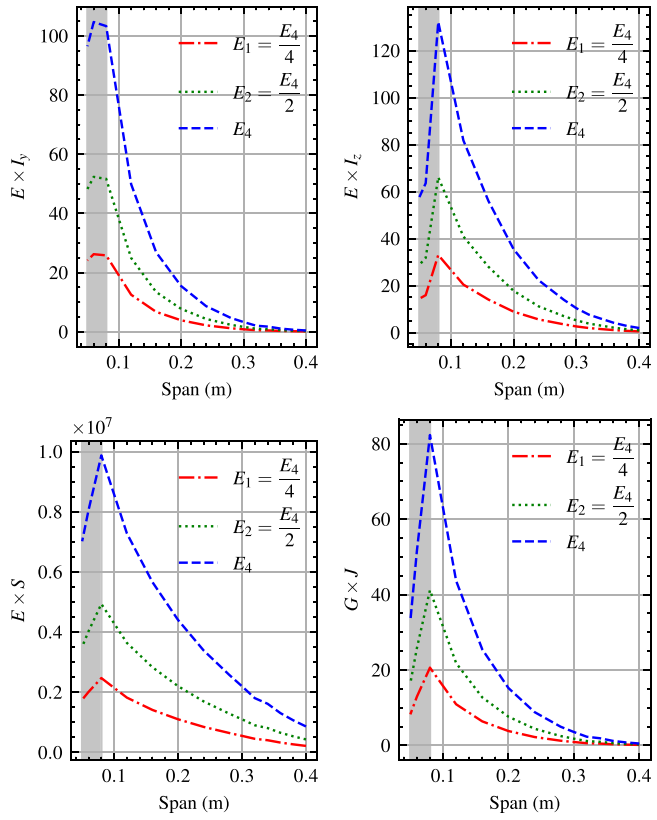

Fig. 7. Structural properties of the beam along the span of the blade.

Table 5
Notation for the structure properties.

Symbol	Description
E	Young modulus (Pa)
ν	Poisson's ratio
$G = E/(2(1+\nu))$	shear modulus (Pa)
S	section surface of the structure (m^2)
I_y	second moment of inertia for bending flap wise (around y, m^4)
I_z	second moment of inertia for bending rotation wise (around z, m^4)
J	polar moment of inertia (around x, m^4)

deteriorates significantly with decreasing stiffness, for the same reason.

Fig. 9 shows the deformed blade for the different Young moduli at TSR 5. E_1 has the biggest deflection, and is quite unrealistic. The deflection occurs both in the direction of flow and in the direction of rotation.

4.3. Blade-mast dynamic interaction with FSI

A mast is added to the computation domain. The mast is considered rigid, and the hub split into two parts. The first part is fixed and linked to the mast, and the second part is rotating with the blades. As previously, the domain is split into two domains, but the fixed domain now includes the mast and a portion of the hub now. An outline of the mesh is shown in Fig. 10. This mesh consists of 7.9 million cells.

We chose to consider E_4 and E_2 only, because E_1 showed poor performance results and was therefore considered unrealistic (see Section 4.2). We used a time step of 10^{-3} s, which is lower than a $\frac{1}{200^{th}}$ of a rotation period.

The water turbine is rotating at 21.625 rad/s which corresponds to TSR 5. The frequency of the blade passage in front of the mast is 3.44 Hz.

We record the position and forces on all structural nodes of the blade.

Acceleration at the tip of the blade is shown in Fig. 11. The start of the graph shows the recovery after passing in front of the mast. At $t = 3.78$ s, the blade arrives near the mast. The acceleration reaches 30 m/s^2 for E_2 and 15 m/s^2 for E_4. The recovery starts with an acceleration peaking at 8 m/s^2 for E_2 and 6 m/s^2 for E_4 at $t = 3.82$ s for E_2 and 3.81 s for E_4. The time for recovery (acceleration of 0 m/s^2) is approximately the same and take 0.17 s. A cycle takes 0.29 s at TSR 5. The first acceleration and its recovery takes ≈ 60% of a cycle. For larger TSR, this would be even more noticeable.

Fig. 12 shows the linear force compared to the average force on different sections of the blade. Upper and middle sections show a similar behavior: there is a spike in relative negative force when going past the mast and a recovery afterward. The bottom portion is much more chaotic which is due to vortex shedding. The upper blade portion shows some difference between E_2 and E_4 while for the middle portion this difference is less noticeable. For the upper blade portion, the difference between E_2 and E_4 is 2.5 N/m at $t = 3.75$ s and is almost 0 N/m during recovery.

Fig. 13 shows the absolute forces acting on each structural node of the blade. The loading is the greatest at the center of the beam (23 N at $r = 0.25$ m) and the lowest at the root of the blade (0.3 N). Furthermore, the loading extends further on the upper part of the blade than on the lower part of the blade. On the upper part of the beam the loading is almost constant and approximately 15 N (from $r = 0.3$ m to $r = 0.38$ m) and on the lower part of the beam it evolves almost linearly between the maximum value of 23 N–0.3 N at the root of the blade. It is difficult to see a transient behavior. Between E_2 and E_4, it is also very difficult to notice a difference.

Fig. 14 shows the difference between the fluid force and overall time averaged force for each structural node of the blade over time. With this post-processing, it is easier to see the transient behavior. For blade radii greater than $r = 0.1$ m, there is a negative spike in forces just at the passage of the mast. It is then recovered with a more continuous positive pressure. The negative spike occurs on the whole blade, especially for E_4, the upper part for E_2 being less spiky. There are very fluctuating forces at the root of the blade.

Fig. 15 shows the Fourier transform of the forces in the frequency space. for E_2 and E_4 the frequency corresponding to the rotation frequency are highly excited as expected. The second mode (≈7 Hz) is higher for E_2 than for E_4. It is the contrary for the third mode (≈10.3 Hz). The fourth mode (≈14 Hz) is existent in E_2 but barely present for E_4. At the root of the blade, the frequency we can see are related to the vortices advected in the flow.

Fig. 16 shows the acceleration of each structural node of the blade. The acceleration is the greatest at the tip of the blade, as one should expect. As seen before, the acceleration peak is half the magnitude for E_4 compared to E_2. The most interesting feature is the positive acceleration after the peak, called here recovery, which is shorter in duration when the stiffness is higher. For E_2, the acceleration is non-negligible for a large portion of the cycle, while for E_4 it concerns less than half of the cycle.

Fig. 17 shows the Fourier transform of the acceleration for each structural node of the blade. It is scaled radius by radius to show which mode is excited for each configuration. For E_2, the first mode – which is the frequency of rotation 3.44 Hz – is highly excited, while for E_4 it is less the case. The second mode (≈7 Hz) is the principal mode to be excited for E_4 and is also excited for E_2. The third mode (≈10 Hz) is highly excited for E_2. The fourth mode (≈14 Hz) is much more excited for E_4 than E_2. There is not a huge difference in spectrum between the tip and the root except for very high frequencies.

Fig. 18 is showing the vortices in the domain using the Q criterion (TSR 5 and E_2). A zoom at the root of the blade shows a vortex due to the cylindrical shape at this section. As stated before, the vortex oscillation at the root of the blade has a different frequency than the rotation frequency.

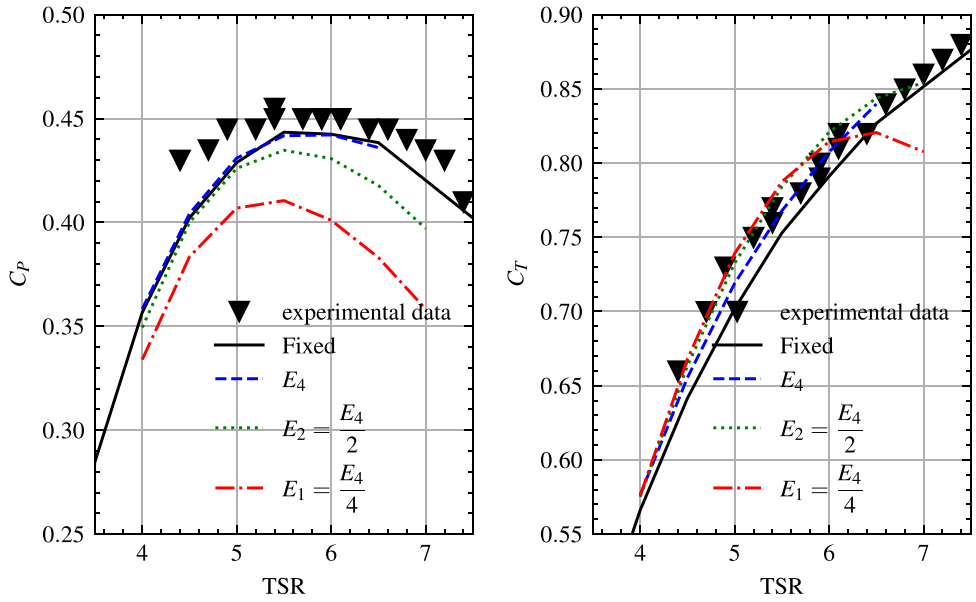

Fig. 8. Performance curves for different structural properties.

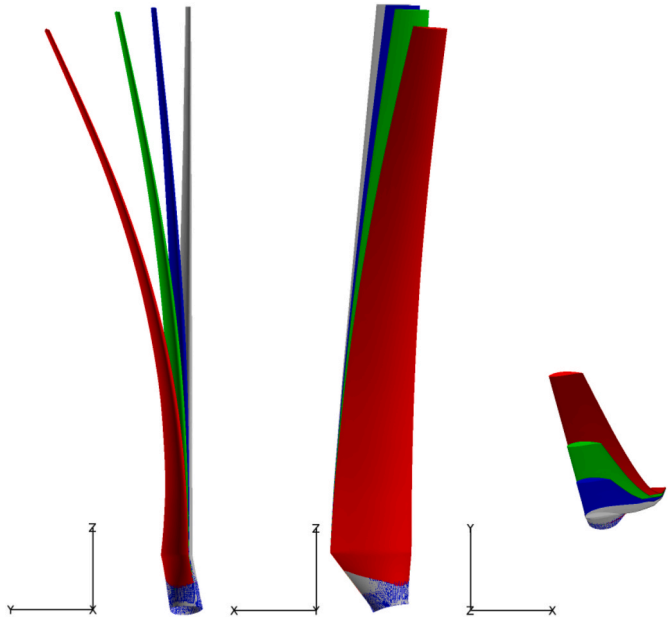

Fig. 9. Different views of deformed blades (grey: fixed, blue:E_4, green:E_2, red: E_1). The left figure is from the turbine side, the middle figure shows the rear view, and the right figure shows the top view. (For interpretation of the references to colour in this figure legend, the reader is referred to the Web version of this article.)

Fig. 19 shows a cut of the mesh showing the deformed mesh. The sliding interface is treated as non-deformable mesh morphing algorithm.

5. Conclusion

A dynamic methodology has been developed to perform fluid computations and was validated against results from Batten et al. (2007). The results show a good agreement with the experiment especially for the design pitch angle of 20° where the error is minimal. In order to use a dynamic rotating mesh, a criterion for the time stepping rule was found.

Three different structures were setup and simulated using quasi-

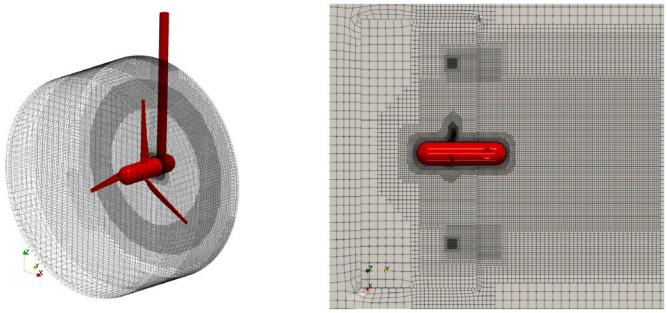

Fig. 10. Different views of the initial fluid mesh for the blade-mast dynamic interaction. The figure on the left shows the sliding interface with the mesh rotating in the inner cylinder and the rest is remaining fixed. The figure on the right shows a slice of the mesh viewed from the top.

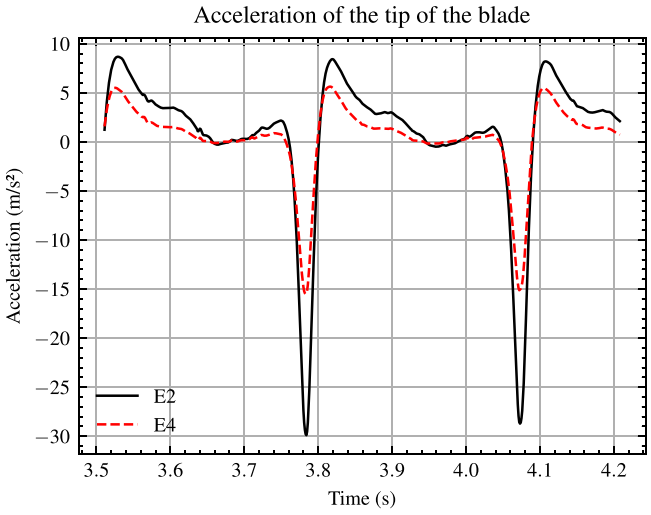

Fig. 11. Acceleration of the tip of the blade (in m/s^2).

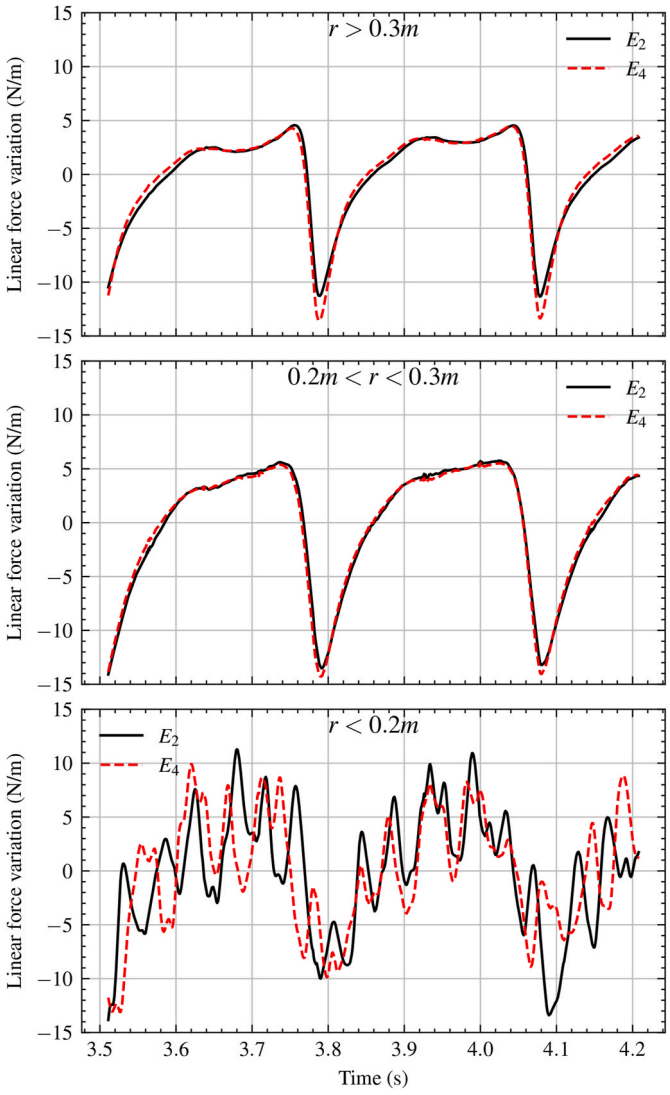

Fig. 12. Linear force compared to average linear force on different sections of the blade (in N/m).

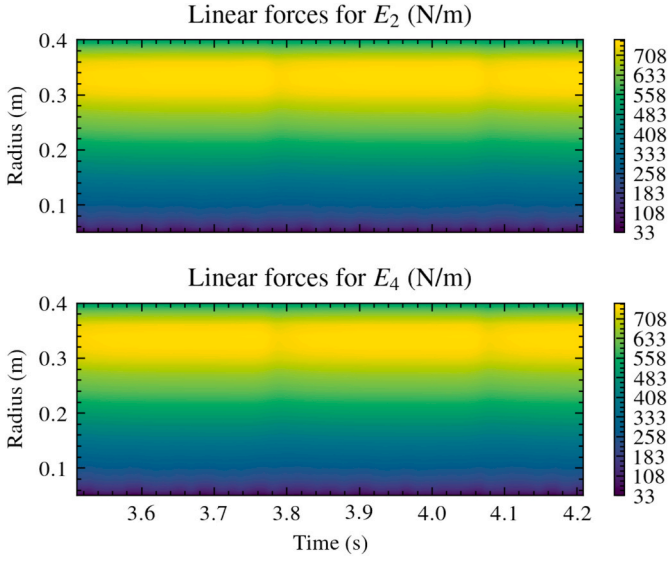

Fig. 13. Linear force on the blade according to time (in N/m).

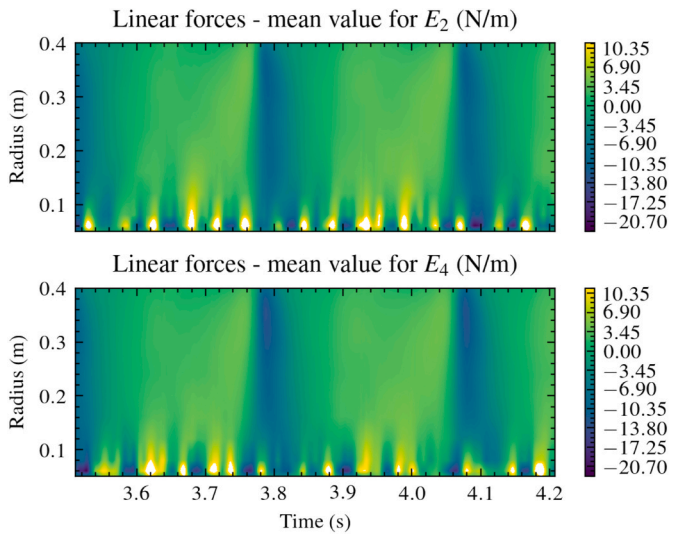

Fig. 14. Linear force compared to average forces acting on the blade according to time (in N/m).

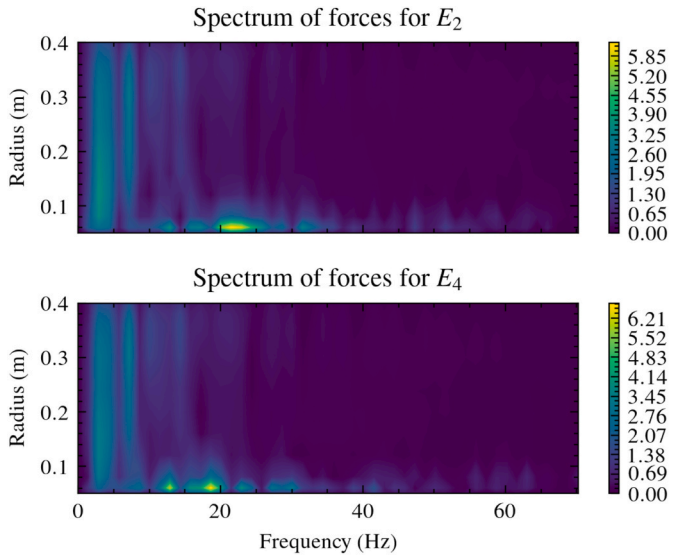

Fig. 15. Frequency analysis of forces acting on the blade.

static fluid-structure computations. The difference between a flexible and a rigid blade was most evident at a TSR greater than 5. These cases excluded the most flexible blade (E_1) for the rest of the study because it produced a poor power curve and thus did not seem suitable for production.

E_2 and E_4 were then setup with a mast. The rotation of the blades in front of the mast induced vibrations. The vibrations and forces were recorded for comparison. Different behaviors were highlighted. The most flexible of the two structures (E_2) showed the greatest displacements and accelerations but the lowest vibrational frequencies.

For future work, wave induced vibrations could be introduced. There are already some experimental work done in this area, for example Luznik et al. (2013); Gaurier et al. (2013). An optimization based on fatigue analysis could help to maximize the durability of such a turbine. For example, the recent work of Finnegan et al. (2020) shows the interest of fatigue loading for tidal turbines. It would also be very interesting to compare against experimental data.

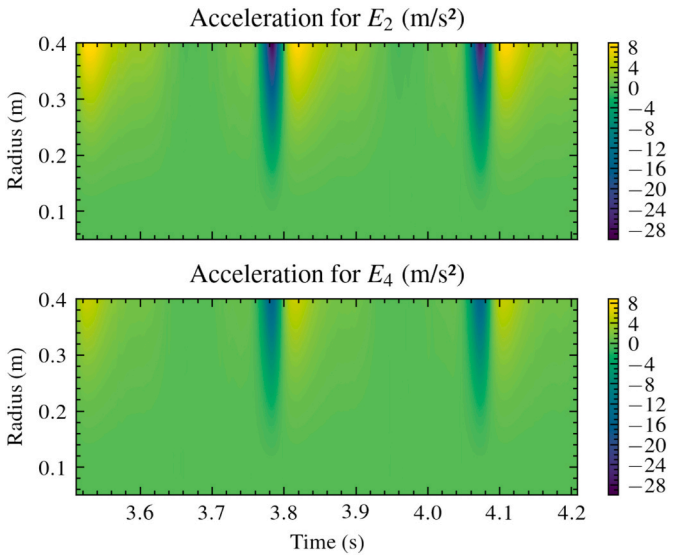

Fig. 16. Acceleration of each structural node of the blade according to time (in m/s^2).

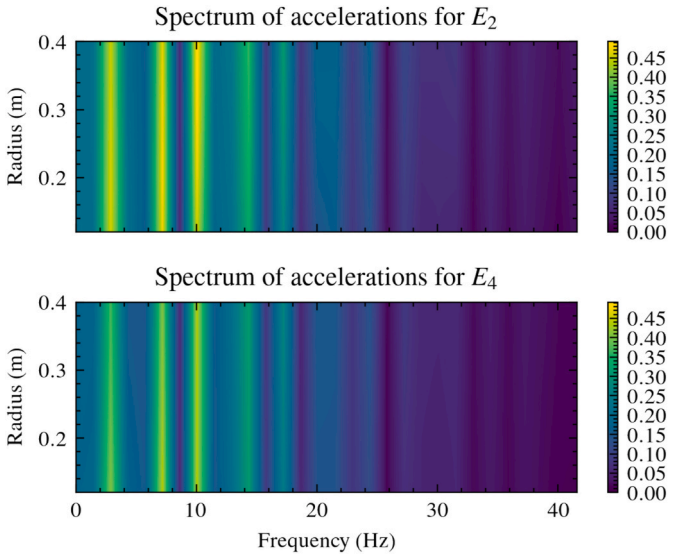

Fig. 17. Frequency analysis of acceleration of each blade element blade.

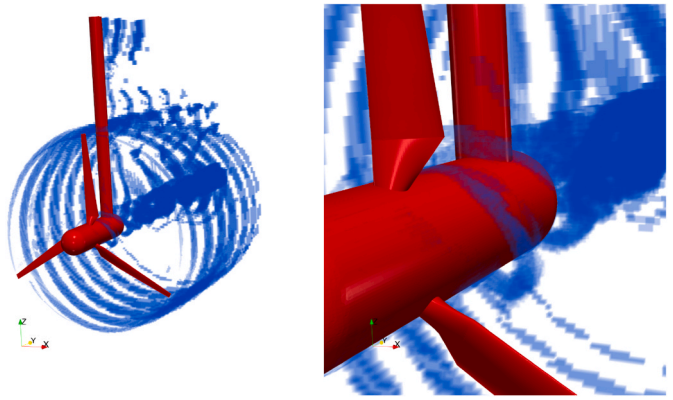

Fig. 18. Instant view of the simulation showing the Q criterion > 100.

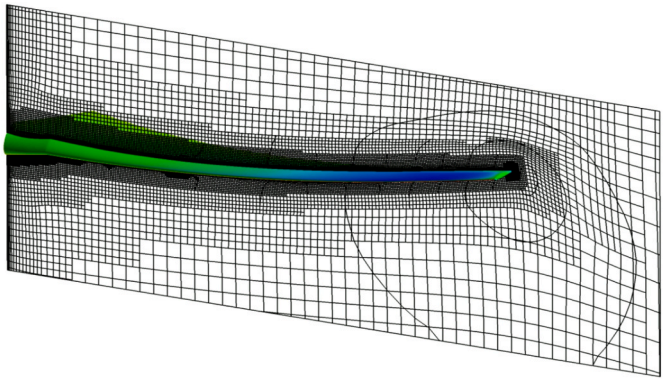

Fig. 19. View of the deformed mesh along the blade.

CRediT authorship contribution statement

Corentin Lothode: Writing, Investigation, Software. **Jules Poncin:** Methodology, Validation, Investigation. **Didier Lemosse:** Supervision, Conceptualization. **David Gross:** Writing, Investigation, Resources. **Eduardo Souza de Cursi:** Funding acquisition, Supervision.

Declaration of competing interest

The authors declare that they have no known competing financial interests or personal relationships that could have appeared to influence the work reported in this paper.

Data availability

Data will be made available on request.

Acknowledgment

This work was initially funded by K-Epsilon and the ANRT via a CIFRE doctoral grant and a partnership with the LMN of INSA Rouen. K-Epsilon supported the project through a partnership with LMRS –CNRS. We are thankful for the computing support provided by CRIANN. We would like to thank NUMECA International, now Cadence, for the R&D license.

Appendix A. Supplementary data

Supplementary data to this article can be found online at https://doi.org/10.1016/j.oceaneng.2022.112046.

References

Afgan, I., McNaughton, J., Rolfo, S., Apsley, D., Stallard, T., Stansby, P., 2013. Turbulent flow and loading on a tidal stream turbine by LES and RANS. Int. J. Heat Fluid Flow 43, 96–108.

Bahaj, A., Molland, A., Chaplin, J., Batten, W., 2007. Power and thrust measurements of marine current turbines under various hydrodynamic flow conditions in a cavitation tunnel and a towing tank. Renew. Energy 32, 407–426.

Batten, W., Bahaj, A., Molland, A., Chaplin, J., Group, S.E.R., et al., 2007. Experimentally validated numerical method for the hydrodynamic design of horizontal axis tidal turbines. Ocean Eng. 34, 1013–1020.

Bazilevs, Y., Hsu, M.C., Kiendl, J., Wüchner, R., Bletzinger, K.U., 2011. 3d simulation of wind turbine rotors at full scale. part ii: fluid–structure interaction modeling with composite blades. Int. J. Numer. Methods Fluid. 65, 236–253.

Calaf, M., Meneveau, C., Meyers, J., 2010. Large eddy simulation study of fully developed wind-turbine array boundary layers. Phys. Fluid. 22, 015110.

Causin, P., Gerbeau, J.F., Nobile, F., 2005. Added-mass effect in the design of partitioned algorithms for fluid–structure problems. Comput. Methods Appl. Mech. Eng. 194, 4506–4527.

Deng, G., Guilmineau, E., Queutey, P., Visonneau, M., 2005. Ship flow simulations with the isis cfd code. In: CFD Workshop, pp. 474–482. Tokyo.

Derakhshan, S., Ashoori, M., Salemi, A., 2017. Experimental and numerical study of a vertical axis tidal turbine performance. Ocean Eng. 137, 59–67.

Durand, M., 2012. Interaction fluide-structure souple et legere, application aux voiliers. Ph.D. thesis Ecol. Cent. Nantes.
Durand, M., Leroyer, A., Lothodé, C., Hauville, F., Visonneau, M., Floch, R., Guillaume, L., 2014. Fsi investigation on stability of downwind sails with an automatic dynamic trimming. Ocean Eng. 90, 129–139.
Duvigneau, R., Visonneau, M., Deng, G.B., 2003. On the role played by turbulence closures in hull shape optimization at model and full scale. J. Mar. Sci. Technol. 8, 11–25.
Fernández, M.A., 2011. Coupling schemes for incompressible fluid-structure interaction: implicit, semi-implicit and explicit. SeMA J. 55, 59–108.
Fernández, M.Á., Moubachir, M., 2005. A Newton method using exact jacobians for solving fluid–structure coupling. Comput. Struct. 83, 127–142.
Fernandez-Rodriguez, E., Stallard, T., Stansby, P., 2014. Experimental study of extreme thrust on a tidal stream rotor due to turbulent flow and with opposing waves. J. Fluid Struct. 51, 354–361.
Finnegan, W., Fagan, E., Flanagan, T., Doyle, A., Goggins, J., 2020. Operational fatigue loading on tidal turbine blades using computational fluid dynamics. Renew. Energy 152, 430–440.
Funke, S.W., Farrell, P.E., Piggott, M., 2014. Tidal turbine array optimisation using the adjoint approach. Renew. Energy 63, 658–673.
Gaurier, B., Davies, P., Deuff, A., Germain, G., 2013. Flume tank characterization of marine current turbine blade behaviour under current and wave loading. Renew. Energy 59, 1–12.
Gross, D., 2015. New quasi-monolithic method to solve dynamic fluid-structure interaction problems on membranes. In: Textiles Composites and Inflatable Structures VII: Proceedings of the VII International Conference on Textile Composites and Inflatable Structures, vols. 19–21. CIMNE, Barcelona, Spain, pp. 344–355. October, 2015.
Hughes, T.J., Liu, W.K., Zimmermann, T.K., 1981. Lagrangian-eulerian finite element formulation for incompressible viscous flows. Comput. Methods Appl. Mech. Eng. 29, 329–349.
de Jesus Henriques, T., Tedds, S., Botsari, A., Najafian, G., Hedges, T., Sutcliffe, C., Owen, I., Poole, R., 2014. The effects of wave–current interaction on the performance of a model horizontal axis tidal turbine. Int. J. Mar. Energy 8, 17–35.
Jimenez, A., Crespo, A., Migoya, E., Garcia, J., 2007. Advances in large-eddy simulation of a wind turbine wake. In: Journal of Physics: Conference Series. IOP Publishing., 012041
Jonkman, J., 2010. Nwtc Design Codes (Fast). NWTC Design Codes (FAST). NREL, Boulder, CO.
K-Epsilon, 2020. K-epsilon website. http://www.k-epsilon.com.
Khan, M., Bhuyan, G., Iqbal, M., Quaicoe, J., 2009. Hydrokinetic energy conversion systems and assessment of horizontal and vertical axis turbines for river and tidal applications: a technology status review. Appl. Energy 86, 1823–1835.
Küttler, U., Wall, W.A., 2008. Fixed-point fluid–structure interaction solvers with dynamic relaxation. Comput. Mech. 43, 61–72.
Leroyer, A., Visonneau, M., 2005. Numerical methods for RANSE simulations of a self-propelled fish-like body. J. Fluid Struct. 20, 975–991.
Lothodé, C., 2018. Modélisation des pales d'éoliennes ou d'hydroliennes en environnement naturel à l'aide d'un code fluide-structure. Ph.D. thesis. Normandie.
Lothodé, C., Durand, M., Roux, Y., Leroyer, A., Visonneau, M., Dorez, L., Team, G.S., 2013. Dynamic fluid structure interaction of a foil. Innov'Sail 1–6.
Lothodé, C., Fontaine, G., Guilmineau, E., Wang, A., Vertallier, F., Minguez, M., Cinello, A., 2015. Numerical study of viv over a flexible riser. In: Marine 2015, VI International Conference on Computational Methods in Marine Engineering.
Luznik, L., Flack, K.A., Lust, E.E., Taylor, K., 2013. The effect of surface waves on the performance characteristics of a model tidal turbine. Renew. Energy 58, 108–114.
Murray, R.E., Thresher, R., Jonkman, J., 2018. Added-mass effects on a horizontal-axis tidal turbine using fast v8. Renew. Energy 126, 987–1002.
Mycek, P., Gaurier, B., Germain, G., Lothodé, C., Pinon, G., Rivoalen, E., 2013. Numerical and experimental characterisation of interactions between two marine current turbines. Rev. Paralia 6.
Mycek, P., Gaurier, B., Germain, G., Pinon, G., Rivoalen, E., 2014. Experimental study of the turbulence intensity effects on marine current turbines behaviour. part i: one single turbine. Renew. Energy 66, 729–746.
Nicholls-Lee, R., Turnock, S., Boyd, S., 2013. Application of bend-twist coupled blades for horizontal axis tidal turbines. Renew. Energy 50, 541–550.
Nicholls-Lee, R.F., 2011. Adaptive Composite Blades for Horizontal axis Tidal Turbines. Ph.D. thesis. University of Southampton.
Numeca, 2018. Theory Manual of FINE/Marine.
Pinon, G., Mycek, P., Germain, G., Rivoalen, E., 2012. Numerical simulation of the wake of marine current turbines with a particle method. Renew. Energy 46, 111–126.
Queutey, P., Deng, G., Wackers, J., Guilmineau, E., Leroyer, A., Visonneau, M., 2012. Sliding grids and adaptive grid refinement for RANS simulation of ship-propeller interaction. Ship Technol. Res. 59, 44–57.
Stallard, T., Collings, R., Feng, T., Whelan, J., 2013. Interactions between tidal turbine wakes: experimental study of a group of three-bladed rotors. Phil. Trans. Math. Phys. Eng. Sci. 371, 20120159.
Takizawa, K., Henicke, B., Montes, D., Tezduyar, T.E., Hsu, M.C., Bazilevs, Y., 2011. Numerical-performance studies for the stabilized space–time computation of wind-turbine rotor aerodynamics. Comput. Mech. 48, 647–657.
Tedds, S., Owen, I., Poole, R., 2014. Near-wake characteristics of a model horizontal axis tidal stream turbine. Renew. Energy 63, 222–235.
Verbeek, M.C., Labeur, R.J., Uijttewaal, W.S., 2020. Estimating the stability of a bed protection of a weir-mounted tidal turbine. Int. Mar. Energy J. 3, 21–24.
Wang, Q., Sprague, M.A., Jonkman, J., Johnson, N., Jonkman, B., 2017. BeamDyn: a high-fidelity wind turbine blade solver in the fast modular framework. Wind Energy 20, 1439–1462.
Wood, W., Bossak, M., Zienkiewicz, O., 1980. An alpha modification of newmark's method. Int. J. Numer. Methods Eng. 15, 1562–1566.
Yan, J., Deng, X., Korobenko, A., Bazilevs, Y., 2017. Free-surface flow modeling and simulation of horizontal-axis tidal-stream turbines. Comput. Fluid 158, 157–166.
Zilic De Arcos, F., Vogel, C., Willden, R.H., 2019. Hydrodynamic modelling of flexible tidal turbine blades. In: European Wave and Tidal Energy Conference 2019, Technical Committee of the European Wave and Tidal Energy Conference.